



## Gaussian filtering method of evaluating the elastic/elasto-plastic properties of sintered nanocomposites with quasi-continuous volume distribution



Yutai Su<sup>a</sup>, Ziyi Shen<sup>a</sup>, Xu Long<sup>a,\*</sup>, Chuantong Chen<sup>b</sup>, Lehua Qi<sup>c</sup>, Xujiang Chao<sup>c,\*\*</sup>

<sup>a</sup> School of Mechanics, Civil Engineering and Architecture, Northwestern Polytechnical University, Xi'an, 710072, PR China

<sup>b</sup> Institute of Scientific and Industrial Research, Osaka University, Osaka, Japan

<sup>c</sup> School of Mechanical Engineering, Northwestern Polytechnical University, Xi'an, 710072, China

### ARTICLE INFO

#### Keywords:

Metal matrix nanocomposites  
Gaussian random field  
RVE  
Quasi-continuous matrix  
Elastic/elasto-plastic properties

### ABSTRACT

In this work, combining the Gaussian filtering algorithm and the cutting quantile functions, a new technique is developed to efficiently generate the RVE of randomly distributed metal matrix nanocomposites (MMNCs) with quasi-continuous volume distribution. The procedures of filtering the random point matrix, generating the random field, separating the spatial points into constituents, and imposing the periodic boundary conditions are numerically implemented in detail. By contrasting the elastic/elasto-plastic properties of the sintered AgNPs composites with those determined by experimental measurements and analytical models, the proposed numerical homogenization model is verified. The results show that the proposed algorithm can control the distributions of the reinforcement size and the matrix volume fractions by tailoring the Gaussian widths and cutting levels. Meanwhile, the ratio of the Gaussian widths to the RVE length  $\sigma/L$  make influences on the resulting elastic/elasto-plastic properties of the MMNCs, and for the sintered AgNPs composites,  $\sigma/L = 2.5$  is the critical value of its convergence. Additionally, the proposed method can be also extended to predict the other physical properties of MMNCs including conduction and diffusion.

### 1. Introduction

Due to the excellent mechanical, electrical and thermal properties [1, 2], metal nanocomposites (MMNCs), such as alloy/nanotube/graphene particle-reinforced composites and sintered dual-phase nanoparticles composites [3,4], have been successfully applied in aerospace, automotive, transportation, and battery electrode. Since it has been proven that the mechanical properties of MMNCs are determined by its microstructures [5,6], an emerging class of MMNCs exhibiting ultra-mechanical properties at harsher environment are enabled by combining and tailoring the properties of their two/multi constituents and microstructures, such as strength and stiffness of the reinforcements, ductility, and toughness of the matrix [7,8]. Therefore, to fully explore the potential design space of the MMNCs with ultra-mechanical properties, it is necessary to understand the relationship between microstructure and mechanical properties.

Compared with the experimental investigations, characterized as time-consuming and expensive, the predictive model, which at least can be considered as the alternative to complement the experimental

measurements, is realized by applying the numerical methods to make assumptions in the mechanical field such as stress/strain or the microstructures of the composites [9,10]. Generally, mean-field and numerical homogenization are the two most common approaches to predict the effective mechanical based on the microstructures of the real composites [11,12]. It is accepted that the numerical homogenization methods are needed to obtain more accurate priority results of the effective mechanical properties of composites, especially when the micro field distributions of the composites with complex microstructures or non-linear constituents of the components are necessary to know [13,14]. To implement the numerical homogenization strategy, the microstructures of the MMNCs are often described using RVEs [15]. Generally, the RVE should be large enough to contain more information about the materials [16,17]. However, Drugan and Willis [18] assert that the RVE also should be the smallest volume of the composites for which the resulting mechanical behaviors remain constitutively valid.

Recently, researchers have developed various methods to generate the RVE of MMNCs with microstructures of spheroidal, ellipsoidal and polyhedral particles [19], such as the Monte Carlo algorithm, random sequential adsorption (RSA) algorithm, Gaussian random field (GRF),

\* Corresponding author.

\*\* Corresponding author. School of Mechanical Engineering, Northwestern Polytechnical University, Xi'an, 710072, China.

E-mail addresses: [xulong@nwpu.edu.cn](mailto:xulong@nwpu.edu.cn) (X. Long), [qilehua@nwpu.edu.cn](mailto:qilehua@nwpu.edu.cn) (L. Qi), [xchao\\_me@nwpu.edu.cn](mailto:xchao_me@nwpu.edu.cn) (X. Chao).

Nomenclature	
$\sigma$	Gaussian width of the Gaussian kernel
$L$	Length of the RVE
$X(s; \omega)$	Initial random point matrix in the probability space
$s$	Spatial locations in the 3D integer domain $D$ ( $L \times L \times L$ )
$\Omega$	Sample space
$\omega$	State index of the sample space
$D$	Integer domain
$G_i$	Gaussian kernel
$Z$	Random point matrix
$g_j(u_j, v_j, w_j)$	Gaussian kernel point in $x$ , $y$ , and $z$ directions
$p_i(u_i, v_i, w_i)$	Target point in $x$ , $y$ , and $z$ directions
$d_{uj}, d_{vj}, d_{wj}$	Distances between the Gaussian kernel point and the target point
$I(p)$	Indicator function in the spatial domain
$Q(\varphi)$	Quantile function or Cutting level
$\varphi$	Volume fraction
$z$	Unordered vector
$z_{(k)}$	The $k$ th ordered in random point matrix $Z$
MAPE	Mean absolute percentage error
$S_2(r_i)$	Two-point probability function
$r_i$	Distance between any two points $p_1$ and $p_2$
$u$	Displacement field
$u_i^0$	Linear displacement/strain field in the periodic domain
$\psi^{th}$	Boundary surface
$\psi^+, \psi^-$	Two parallel opposites surfaces
$P_j^{\psi^+} - P_j^{\psi^-}$	Constant for nodes pair on the parallel boundary
$\tilde{\varepsilon}_{ij}$	Macroscopic strain
$\sigma_{ii}, \sigma_{jj}$	Stress in the direction $i$ and $j$
$E$	Elastic modulus
$R$	Hardening coefficient
$n$	Hardening exponent
$\varepsilon_y$	Yield strain
$\sigma_y$	Yield stress
$E_{\max}, E_{\min}$	Maximum and minimum elastic properties
$N_{RVEs}$	Number of the RVEs
$E_{Ag}, V_{Ag}$	Elastic modulus and Poisson's ratio of bulk silver

and non-Gaussian random field (n-GRF) [20,21]. Diverse composite materials are obtained by thoroughly combining constituents with distinct material structures using specific processing techniques [22,23]. Subsequently, numerous works utilize spatial statistical methods to describe these intricate material distributions [24,25]. Jahed et al. [26] developed a quantitative evaluation of particle size and dispersion in metal-matrix composite and applied it to investigate the homogeneity and microstructural distribution of Cu-matrix composites. Based on the understanding of the particle distributions, Tian et al. proposed a modified RSA algorithm to efficiently generate the RVE of spheroidal particles reinforced MMNCs with specified orientations [27]. Although this method has broken through the volume fraction limitation of the fillers, the stress concentration indescribable and pseudo-random distribution of the particles is still challenging. In addition, some open-source packages can also be used to generate the RVE with a polyhedral grain structure such as *Dream3D*, *Moose* and *Openphase* [28, 29]. Gao et al. [19] generate the RVE of SiC particles with array network architecture based on the experimental observations and *Neper* package [30]. However, the volume fraction here is a fixed proportion with weak adjustability. GRF is a statistical continuous probability distribution, and by using the decomposed Karhunen-Loève extension method, Gao et al. [20] established an explicit random field model that can describe the RVE of MMNCs with multi-phase stochastic microstructures. Moreover, based on the multipoint correlation function and Fast Fourier transform, Dehnavi et al. [21] developed an integrated methodology for MMNCs with complex microstructure. However, GRF-based methods are not efficient due to the extraction of the spatially related random numbers. Liu et al. [31] suggested that the  $\beta$  distribution can be used as the edge distribution of second-order n-GRF, but it is only suitable for the material properties with a bounded range. Sintered metal nanoparticles such as silver nanoparticles (AgNPs) are typical MMNCs used for chip packaging with remarkable bonding properties and complex stochasticity microstructures [32]. As the issue involves the RVE generation of these MMNCs, efficiency and low computing-consuming methods are urgently demanded. Sintered metallic nanoparticles, specifically AgNPs, have typical dual-phase microstructures consisting of a solid phase and a pore phase with a random distribution [33,34], which are commonly used in the interconnect structures of wearable electronics and next-generation power electronics [35–37]. Although the macroscopic mechanical properties of AgNPs have been extensively studied [38], the effects of the dual-phase microstructure on the mechanical properties has been overlooked [39].

In this work, a new algorithm combining the Gaussian filtering algorithm and the cutting quantile functions is proposed to efficiently generate the RVE of randomly distributed MMNCs with quasi-continuous matrix. The procedures of the proposed algorithm for filtering the random point data, efficiently generating random field, and separating the spatial points into two-phase are detailedly developed. Statistical analyses are implemented to investigate the size distribution of the reinforcement in the generated RVE. The periodic boundary conditions (PBCs) are applied to obtain the homogenized elastic/elasto-plastic properties and the experimental tests are adopted to validate the proposed method. Moreover, the effects of the Gaussian width on numerical stability are discussed. In the current work, the method is developed to predict the inherent elasto-plastic behaviors, and there is the potential to guide the optimal design of the MMNCs components and to evaluate the onset and progression of damage.

## 2. Random volume element (RVE) generation

### 2.1. Overview of RVE generation algorithm

The proposed algorithm for generating the RVE of the random microstructure is based on the one-cut GRF model and the Gaussian filtering algorithm in image processing. The detailed techniques for generating the RVE of MMNCs are outlined as follows: A discrete cubic matrix with length of  $L$  is constructed in the global Cartesian coordinate system, where the values in the  $x$ ,  $y$ , and  $z$  axes range in  $\mathbb{R} = (0, L]^3$ . Next, the points in the space are discretely assigned as random values to produce spatial point matrix. To ensure an initial random field that is both isotropic and unbiased, point values are drawn independently from a normal distribution  $N(0, 1^2)$ . After that, the random point matrix is filtered using Gaussian kernel with a specified width. The blurred spatial point matrix is still isotropic due to the orientation-independent characteristic of the adopted Gaussian kernel convolution. As the weight of the Gaussian kernel decreases, the blurred individuals become spatially correlated with the Gaussian width. The isotropic point matrix, correlated with its values of the neighboring points, is modeled similarly to the GRF. Further, the cutting level, also known as threshold technique, is specified to create a binary point-matrix with specific proportional constituents, aiming at the target fraction of the real composites. The detailed procedure of the algorithm is shown as Fig. 1. In this method, the initial random field consisting of independent and identically random values with the continuous normal distribution is assigned into

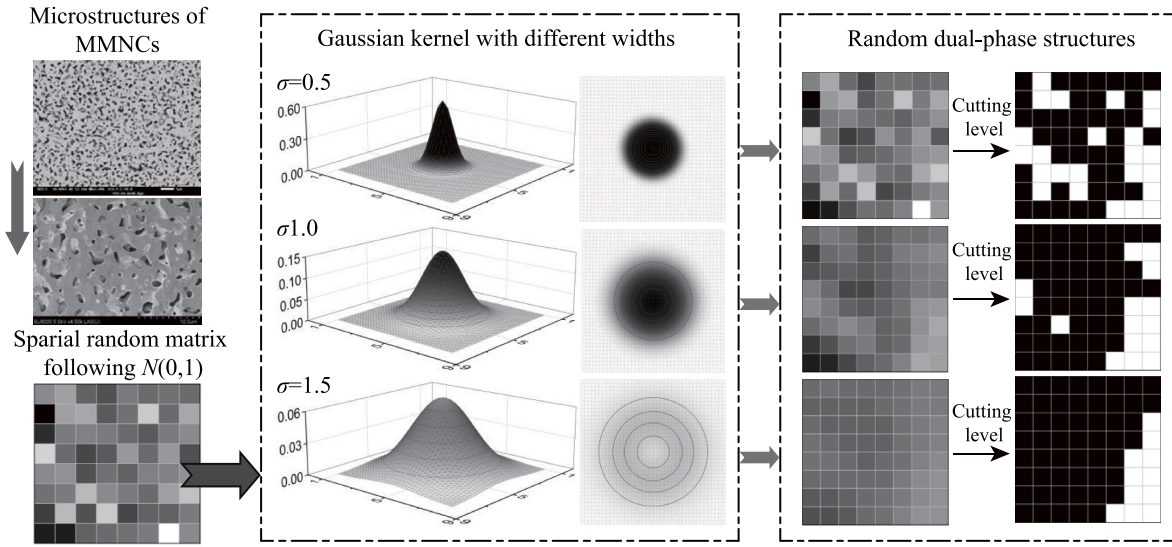


**Fig. 1.** Procedure of the proposed algorithm for generating the RVE of the random microstructural composites.

discrete spatial points. Besides, the continuous Gaussian kernels are also assigned into discrete spatial points. Based on these, the matrix of discrete spatial points is subjected to the Gaussian filtering processes, which are performed in matrix operations, produce a statistically correlated processed random field with high efficiency and rapid computation. Additionally, it is noted that the Gaussian width of the Gaussian kernel is utilized to scale the average size of the target phase cells under the same fraction of composites. And the cutting level is utilized to directly modify the content of the microstructures.

## 2.2. Three-dimensional Gaussian filtering algorithm

The 3D Gaussian filtering algorithm is implemented to quickly construct desirable realizations of the spatial random field. Gaussian filtering algorithm, also called Gaussian smoothing in image processing, uses a spatial kernel that follows Gaussian distribution to convolve a sharp numerical matrix into a smooth one. Fig. 2 shows the procedures of the proposed algorithm. Firstly, a random point matrix with the size of  $L^3$  is created as the initial seed. Then, a Gaussian kernel centered on the coordinates of the target point is generated, and the specified value of the target point is calculated by the matrix convolution. Finally, the assigned values of target points are formed in the target point matrix.

The initial random point matrix in the probability space can be

defined by a 3D spatial random field  $\mathbf{X}(\mathbf{s}; \omega)$  as follow:

$$\{\mathbf{X}(\mathbf{s}, \omega) \in \mathbf{A}_x \subseteq \mathbb{R}; \mathbf{s} \in D \subset \mathbb{Z}^3; \omega \in \Omega\}, \quad (1)$$

where  $\mathbf{s}$  denotes the spatial locations in the 3D integer domain  $D$  ( $L \times L \times L$ ),  $\omega$  is the state index of the sample space  $\Omega$ .  $\mathbf{X}(\mathbf{s}, \omega)$  follows the Gaussian distribution  $\mathbf{N}(0, \mathbf{I})$ . Since each point obeys the consistent probability distribution and the expected value is zero, the realized 3D spatial random field can be considered as isotropic. As a result, the realized  $\mathbf{X}(\mathbf{s}, \omega)$  of the 3D random field, shown as the right of Fig. 1, is served as the input data for the Gaussian filtering algorithm, which could then be used to generate different isotropic point matrices with various widths. It is noted that each location in the 3D random field is independent, which reduces the effects on the Gaussian kernel width and the spatial correlation of the target point matrix.

Within the integer domain  $D$ , 3D Gaussian kernel  $\mathbf{G}_i(g)$  with the Gaussian width  $\sigma$  for a target point  $p_i$  is expressed as:

$$\mathbf{G}_i(g) = \frac{1}{2\pi\sigma^2} e^{-\frac{d_{uij}^2 + d_{vij}^2 + d_{wij}^2}{2\sigma^2}}, \quad (2)$$

where  $d_{uij}$ ,  $d_{vij}$ , and  $d_{wij}$  are the distances between the Gaussian kernel point  $g_j(u_j, v_j, w_j)$  and the target point  $p_i(u_i, v_i, w_i)$  in  $x$ ,  $y$ , and  $z$  directions, respectively, which are written as:

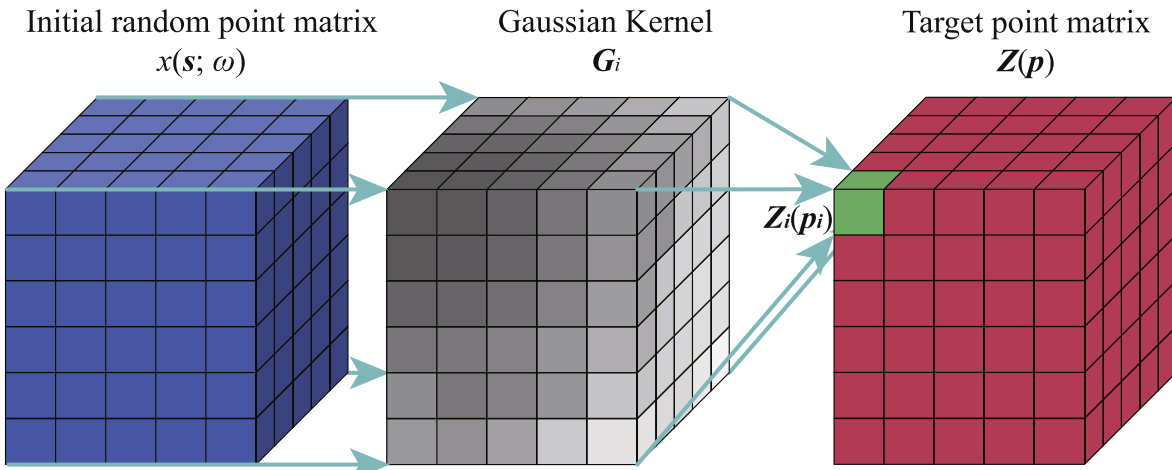


**Fig. 2.** Schematic description of 3D convolution in Gaussian filtering algorithm.

$$d_{uij} = |u_j - u_i|, \quad (3)$$

$$d_{vij} = |v_j - v_i|, \quad (4)$$

$$d_{wij} = |w_j - w_i|, \quad (5)$$

where  $i$  and  $j$  are the number of the target point  $p_i$  and the point  $g_j$  in the Gaussian kernel  $G_i$ . The Gaussian kernel serves as an effective filter when applied to isotropic materials due to its isotropy in the  $x$ ,  $y$ , and  $z$ -directions. Meanwhile, this method can also be used to model anisotropic microstructures using an anisotropic kernel. To generate the microstructures of the anisotropic material, weighted values can be integrated prior to distance calculation in Eqs. (3)–(5). A variety of anisotropic random field can be filtered and generated, as demonstrated in our prior work [34].

The 3D Gaussian kernel  $G_i$  for a specific target point  $p_i$  is presented in the middle of Fig. 2, which acts as a mask with assigned weights. Convolves it with the random seed  $\mathbf{X}(s, \omega)$ , the target point value  $z_i(p_i)$  is derived as:

$$z_i(p_i) = \mathbf{x}(s, \omega) * G_i(\mathbf{g}). \quad (6)$$

Considering the above convolution results, the target point matrix  $\mathbf{Z}(\mathbf{p})$  is composed of all target point values in the integer domain  $D$ . The filtered point matrix is the input data to generate the random dual-phase structures.

Based on the initial random point matrix, a set of filtered point matrices are obtained by varying the Gaussian width. Fig. 3 (a) presents the initial random point matrix with a size of  $50 \times 50 \times 50$ , and Fig. 3 (b)–(f) depict the filtered point matrices with Gaussian widths ranging from 0.5 to 2.5. The RVE unit is dimensionless and not directly tied to a physical length scale because it is a mathematical construct intended for

investigating the behavior of heterogeneous materials and to represent diverse random microstructures. This allows it to be adjusted to match real morphologies. Moreover, the Gaussian width unit is also dimensionless. All the point matrices are overall isotropic. Besides, the Gaussian width  $\sigma$  directly affects the weight distribution of the neighboring points, and the larger the Gaussian width, the larger the transition region between adjacent maxima and minima in the point matrix. Therefore, the size of the particles and monomeric connection regions of a specific phase in the RVE of the random dual-phase composite can be adjusted by the Gaussian width  $\sigma$  of the Gaussian kernel.

### 2.3. Cutting level determination based on the quantile function

The cutting level model is adopted to transform the random point matrix into a binary one, which means dividing the 3D spatial domain into two spatial regions with distinguishable phases. The matrix domain volume fraction is an important parameter for the RVE generation. Here, a quantile function-based approach is developed to determine the cutting level, which could efficiently meet the given volume fraction.

The spatial random point matrix  $\mathbf{Z}(p)$  is sorted from the smallest to largest without regard for its spatial location to yield its order statistics. Assuming that the unordered vector of  $z_1, \dots, z_n$ , where  $n = L^3$ , the  $k$ th ordered  $z_{(k)}$  in random point matrix  $\mathbf{Z}$  is given as:

$$z_{(1)} \leq \dots \leq z_{(k-1)} \leq z_{(k)} \leq z_{(k+1)} \leq \dots \leq z_{(n)}. \quad (7)$$

Then, the cumulative distribution function (CDF) of  $z$  can be written as:

$$F(t) = \Pr\{z \leq t\}. \quad (8)$$

The CDF can be defined as the function of the matrix phase volume fraction. When  $t$  is equal to  $z_{(k)}$ , the volume fraction function is expressed

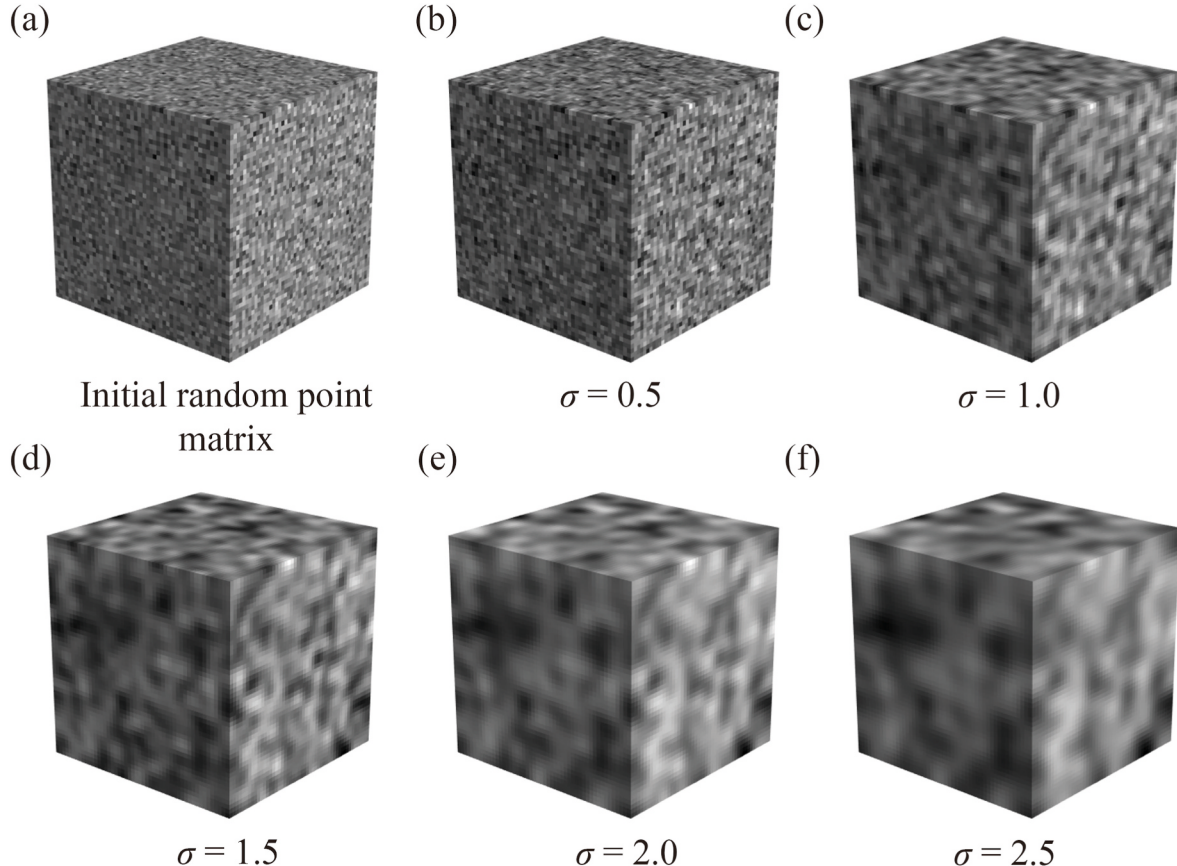


**Fig. 3.** Initial random point matrix (a) and filtered point matrices with various Gaussian widths, (b)  $\sigma = 0.5$ , (c)  $\sigma = 1.0$ , (d)  $\sigma = 1.5$ , (e)  $\sigma = 2.0$ , (f)  $\sigma = 2.5$ .

as:

$$F(z_{(k)}) = \Pr\{z \leq z_{(k)}\} = \frac{k}{n}. \quad (9)$$

Further, the quantile function  $Q(\phi)$ , which is the inverse of the CDF, establishes the mapping from the volume fraction  $\phi$  to the cutting level  $Q$ , also identified as the threshold. The quantile function  $Q(\phi)$  is given as follows:

$$Q(\phi) = F^{-1}(\phi) = \inf\{t : F(t) \geq \phi\} = z\left(\left\lfloor n\phi + \frac{1}{2} \right\rfloor\right), \text{ where } 0 < \phi \leq 1 \quad (10)$$

Therefore, the threshold or the cutting level for a given volume fraction  $\phi$  can be directly calculated by using the quantile function  $Q(\phi)$ . The indicator function  $I(p)$  of the random dual-phase composites in the 3D spatial domain is defined as:

$$I(p) = \begin{cases} 1, & \text{if } z(p) > z\left(\left\lfloor n\phi + \frac{1}{2} \right\rfloor\right) \\ 0, & \text{if } z(p) \leq z\left(\left\lfloor n\phi + \frac{1}{2} \right\rfloor\right) \end{cases} \quad (11)$$

where  $I = 0$  represents the matrix phase and  $I = 1$  represents the

reinforcement phase. Consequently, random dual-phase composites with a specific volume fraction are generated.

**Fig. 4** (a) presents the quantile functions of the random point matrices filtered by Gaussian kernels with different widths  $\sigma$ . As the width of the Gaussian kernel increases, the number of extrema shrinks and the fluctuation of the  $z$ -value distribution reduces in the filtered random point matrix. As a result, for larger Gaussian widths, the quantile function is flatter in the middle. Using the quantile functions with a set of Gaussian widths, RVEs with three types matrix phase volume fractions (0.7, 0.8, and 0.9) are generated to calculate the corresponding cutting levels, as shown by the three vertical lines in **Fig. 4** (a). Moreover, **Fig. 4** (b) depicts the random dual-phase composites with varied volume fractions by different Gaussian kernels. Both the matrix and the reinforcement phase of the generated composites are stochastic in size, shape, and distribution, and the overall random structure is almost isotropic. Under the same matrix-phase volume fraction, with the increase of the Gaussian kernel width, the size of the reinforcement phase is larger while the number of reinforcements decreases. In addition, as the Gaussian kernels are the same and the matrix-phase volume fraction rises, the centers of each reinforcement phase individuals remain nearly constant while the size and number become smaller. By integrating Gaussian filtering with level cutting, it can effectively

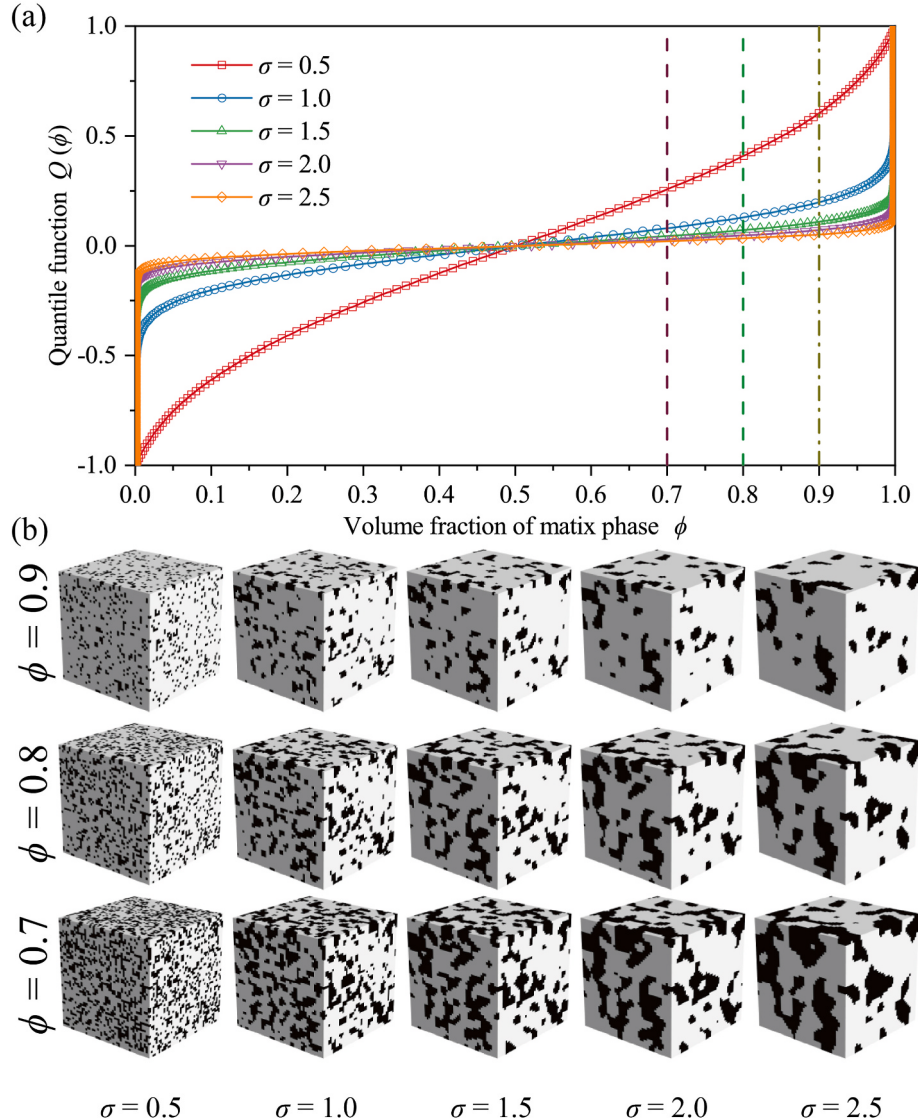


**Fig. 4.** Quantile functions and random structures with different widths and volume fractions.

process 3D discrete point matrices using matrix operations. This approach significantly reduces both computation time and complexity compared to random field generation methods. In addition, as shown in Fig. 4, demonstrate that the generated spatial samples through this approach accurately match the real morphologies. Further statistical analysis is detailed in the subsequent sections.

#### 2.4. Statical analysis of the generated dual-phase RVEs

Using the generated RVEs as a reference, the size of the reinforcement within the RVE of dual-phase composites with varying Gaussian width  $\sigma$  and volume fraction  $\varphi$  are counted and analyzed, as shown in Figs. 5 and 6.

The size of the reinforcement makes significant effect on the elasto-plastic properties of the MMNCs. Therefore, statistics of the reinforcement size is an apparent characteristic of the randomly generated RVEs [40]. With the Gaussian width  $\sigma$  increases, the reinforcement size increases and the frequency distribution shifts to the right, depicted in Fig. 5 (a)–(c). For small reinforcements size ranging from 1 to 10, a larger Gaussian width leads to a lower relative frequency. On the contrary, for reinforcements with the size larger than 100, the increasing Gaussian width tends to increase the relative frequency. Although a smaller matrix volume fraction affects the stability of the aforementioned relationships, the Gaussian width  $\sigma$  could statistically control the number ratio of the reinforcements (small to large), which can generate the RVE with the appropriate frequency characteristic of the reinforcements. Such spatial characteristics resemble those of MMNCs [41–43].

The statistics of the reinforcement size of the RVE with different Gaussian widths and volume fractions are analyzed. In dual-phase microstructures, the reinforcement size corresponds to the non-matrix phase. Maximum, minimum, and average reinforcement size, as well as the total number of reinforcements, are counted to address the statistical characteristics of the reinforcements in the generated RVEs. Here, the average reinforcement size and total reinforcement number have a direct effect on the RVE's stiffness, while the maximum and minimum reinforcement sizes influence the RVE's yield strength and fracture process. Fig. 6 (a) demonstrates the relationships between the maximum reinforcement size and Gaussian width of the RVE with different volume fractions. It is found that the maximum reinforcement size and Gaussian width are roughly positively correlated, and the increase rate slows down when the Gaussian width exceeds a threshold value. For the same Gaussian width, the maximum size increases with the decrease of the volume fraction. In addition, the matrix volume fraction would affect the threshold value. With the increase of the volume fraction, the maximum size does not increase further for the smaller Gaussian widths. The minimum reinforcement size of the RVE is provided in Fig. 6 (b). Generally, the minimum reinforcement size is 1.0. The potential for the minimum reinforcement size increase with the Gaussian width increases. Comparing Fig. 6 (c) and (d), the average reinforcement size and total reinforcement number vary in the different trends regarding the Gaussian width, due to the constant of the total volume of reinforcements in the RVE. As the Gaussian width raises, the average reinforcement size increases while the total reinforcement number drops. Moreover, the matrix volume fractions of the RVE impact negatively the average reinforcement size and positively the overall reinforcement number. Overall, the statistical properties of reinforcements can facilitate the better understanding of the microstructures of the synthetic RVE. Meanwhile, the gaussian width and volume fraction can be used to modify the reinforcement size and quantity of the RVE of MMNCs.

#### 2.5. Microstructure-based RVE generation procedure

The Gaussian kernel and volume fraction have an effect on the reinforcement sizes in synthetic RVE microstructures, particularly for

large and medium-sized reinforcements. Referring our previous work [44] two-point probability function or autocorrelation function  $S_2(\mathbf{r})$  is induced to address the real distribution of the dual-phase sintered nanocomposites, given by

$$S_2(\mathbf{r}) = P\{I(\mathbf{p}_1) = 1, I(\mathbf{p}_2) = 1\} = 1, \quad (12)$$

where  $\mathbf{r}$  is the distance between any two points  $\mathbf{p}_1$  and  $\mathbf{p}_2$  in the microstructure, and  $I(\mathbf{p})$  is an indicator function as Eq. (11).

Using the fast Fourier transformation (FFT) algorithm, it is possible to quantify both the 2D and 3D distribution characteristics of the real or synthetic microstructures. Regarding the proposed generation algorithm, the volume fraction of the RVE must be determined first, followed by the adjustment of the Gaussian kernel of the RVE with a given volume fraction to match the real microstructure. To minimize the difference between the real and the synthetic morphology, the minimum mean absolute percentage error (MAPE) of real and the synthetic  $S_2(\mathbf{r})$  is selected as the optimization problem, resulting in a microstructure-based RVE generation procedure depicted in Fig. 7. Additionally, the python codes are freely provided in GitHub ([github.com/zhanqi-syt/Microstructure-based-RVE-generation-from-2D-to-3D](https://github.com/zhanqi-syt/Microstructure-based-RVE-generation-from-2D-to-3D)).

Fig. 8 (a) shows a real microstructure of sintered metal particles. Through resizing and binary processing, the volume fraction is calculated to be 0.7274, and the two-point probability function  $S_2(\mathbf{r})$  is depicted in Fig. 8 (c). By solving the optimization problem of MAPE between the real and the synthetic two-point probability functions, an acceptable Gaussian width can be obtained to keep the generated RVE's consistency with the real microstructure. Fig. 8 (b) and (c) shows the Generated RVE with a MAPE of 0.005065.

### 3. Periodic geometry model and boundary conditions

Generally, the boundary conditions for predicting the mechanical properties of the composites should satisfy the Hill-Mandel law [16], which ensures that the macroscopic field for the homogenized composites is consistent with the microscopic field for the real composites. And it is proven that the PBCs can more accurately predict the effective elasto-plastic properties of the composites than other boundary conditions such as uniform stress and uniform strain boundary conditions [45]. For the composites of RVE with complex microstructures, the PBCs requires both the opposing parallel surface must satisfy the same meshing pattern. Therefore, the node pairs on the opposing positions should have the same in-plane coordinates. In this work, the RVE is meshed by using the 8-node hexahedral element C3D8, which guarantees that the nodes on the parallel boundary of the surface on the RVE can correspond to each other one by one (Fig. 9 (a)).

The PBCs of the displacement field  $\mathbf{u}$  are applied as linear constraints in ABAQUS under a macroscopic strain is formed as [46]:

$$u_i(x, y, z) = u_i^0 + \tilde{u}_i(x, y, z), \text{ where } u_i^0 = \varepsilon_i^0 P_j, \quad (13)$$

where  $u_i^0$  is the linear displacement/strain field in the periodic domain.  $\tilde{u}_i$  is the periodic part of the displacement/strain field on the surface, and  $i$  represent the freedom in directions of  $x$ ,  $y$  and  $z$ . For the  $\psi^{th}$  boundary surface pair of the two parallel opposite  $\psi^+$  and  $\psi^-$ , the displacements difference between it is written as:

$$u_i^{\psi^+} - u_i^{\psi^-} = \varepsilon_{ij}^0 (P_j^{\psi^+} - P_j^{\psi^-}) = \varepsilon_{ij}^0 \Delta P_j^{\psi}. \quad (14)$$

It should be noted that  $P_j^{\psi^+} - P_j^{\psi^-}$  is constant for each pair of the nodes on the parallel boundary, containing surfaces, vertices and edges in the RVE, shown as in Fig. 9. For a given macroscopic strain  $\tilde{\varepsilon}_{ij}$ , Eq. (14) is constant and therefore the PBCs can be easily applied in the FEA as a nodal displacement constraint. The PBCs on the RVE boundary is driven as:

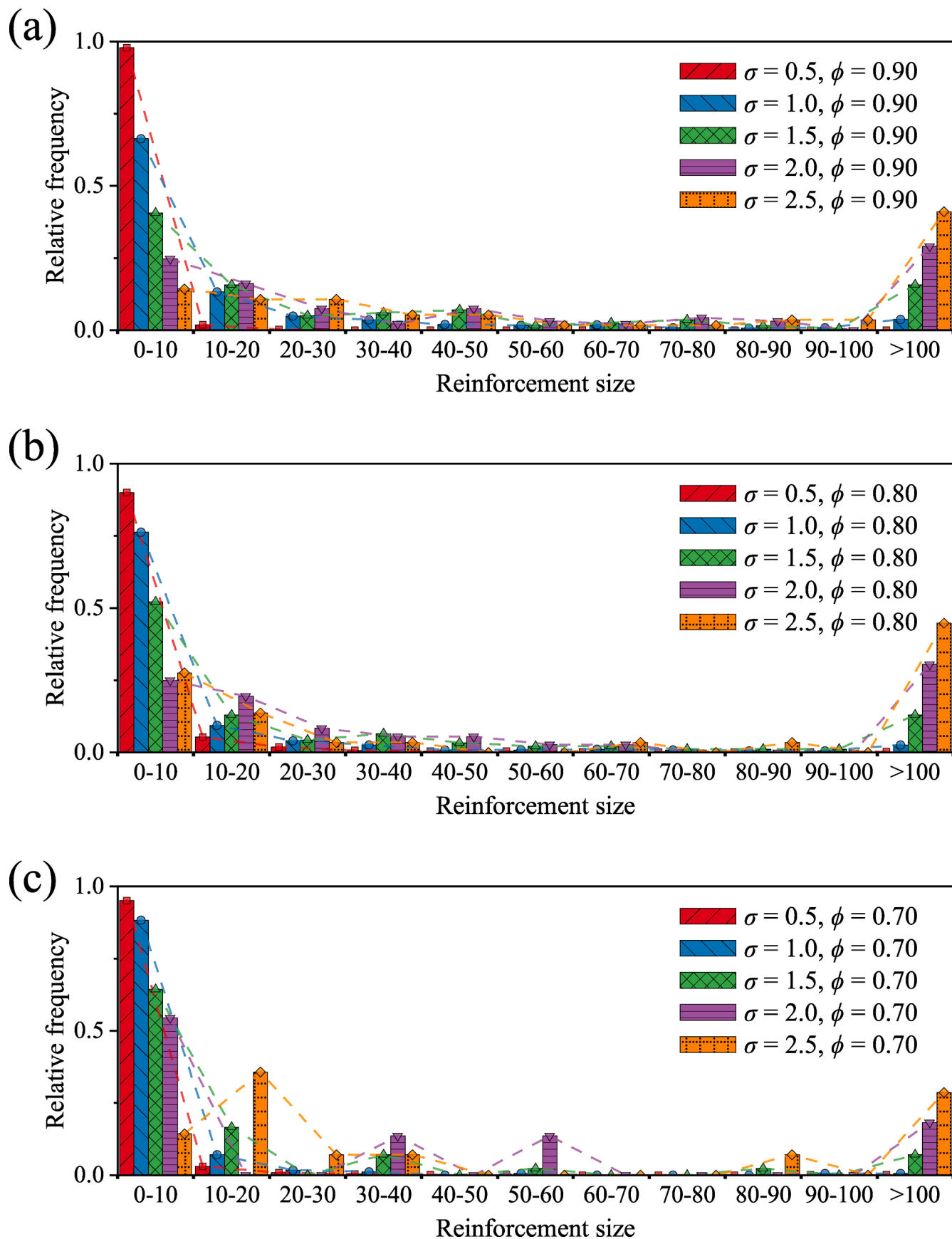
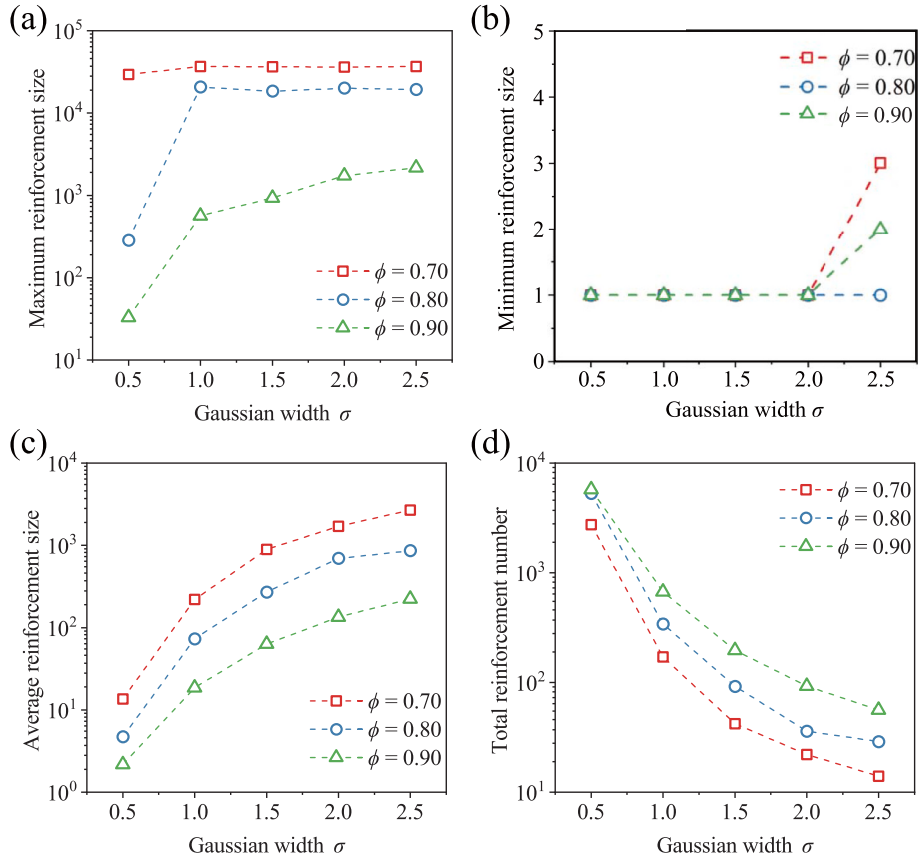


Fig. 5. Statical results of the reinforcement sizes in the RVEs with different volume fractions and Gaussian widths, where (a)  $\phi = 0.90$ , (b)  $\phi = 0.80$ , and (c)  $\phi = 0.70$ .



**Fig. 6.** Statistical characteristics of the reinforcements in the RVE, (a) maximum, (b) minimum, (c) the average reinforcement size, and (d) the total number of reinforcements.

$$u_i^+ - u_i^- = \tilde{\epsilon}_{ij} (P_j^+ - P_j^-) = \Delta u_i. \quad (15)$$

The procedure of imposing the PBC on the boundaries of the RVE by implementing the Python script on the FE package ABAQUS. And the first step is to classify the nodes on the boundaries of the RVE and each node only be featured in one group. Then create the constraint between the node pairs on opposing surfaces.

The nodes on the boundary of the RVE can be divided into three groups: Surfaces nodes S1–S6, edge nodes E1–E12 and vertex nodes V1–V8. Therefore, the detailed implementation equations to apply the PBC in node pairs are given as follows.

#### I. Surface nodes:

##### a. Surface left S1 to Surface right S2:

$$u_i^{CDD1C1} - u_i^{ABB1A1} - \Delta x \epsilon_{ix} = 0, i = x, y, z. \quad (16)$$

##### b. Surface top S4 to Surface bottom S3:

$$u_i^{ABCD} - u_i^{A1B1C1D1} - \Delta y \epsilon_{iy} = 0, i = x, y, z. \quad (17)$$

##### c. Surface front S6 to Surface back S5:

$$u_i^{ADD1A1} - u_i^{BCC1B1} - \Delta z \epsilon_{iz} = 0, i = x, y, z. \quad (18)$$

#### II. Edge nodes:

$$\begin{cases} u_i^{A1B1} - u_i^{CD} - \Delta x \epsilon_{ix} - \Delta y \epsilon_{iy} = 0, \\ u_i^{C1D1} - u_i^{AB} + \Delta x \epsilon_{ix} - \Delta y \epsilon_{iy} = 0, \\ u_i^{A1A} - u_i^{C1C} - \Delta x \epsilon_{ix} - \Delta z \epsilon_{iz} = 0. \end{cases}, \begin{cases} u_i^{D1D} - u_i^{B1B} + \Delta x \epsilon_{ix} - \Delta z \epsilon_{iz} = 0, \\ u_i^{A1A} - u_i^{C1C} - \Delta x \epsilon_{ix} - \Delta y \epsilon_{iy} = 0, \\ u_i^{AD} - u_i^{B1C1} + \Delta y \epsilon_{iy} - \Delta z \epsilon_{iz} = 0. \end{cases} \quad (19)$$

#### III. Vertex nodes:

$$\begin{cases} u_i^{A1} - u_i^C - \Delta x \epsilon_{ix} - \Delta y \epsilon_{iy} - \Delta z \epsilon_{iz} = 0 \\ u_i^{B1} - u_i^D - \Delta x \epsilon_{ix} - \Delta y \epsilon_{iy} + \Delta z \epsilon_{iz} = 0 \\ u_i^{C1} - u_i^A + \Delta x \epsilon_{ix} - \Delta y \epsilon_{iy} + \Delta z \epsilon_{iz} = 0 \\ u_i^{D1} - u_i^B + \Delta x \epsilon_{ix} - \Delta y \epsilon_{iy} - \Delta z \epsilon_{iz} = 0 \end{cases} \quad (20)$$

By assigning each generated dummy node outside the RVE model zone to an equation as Eq. 16–20, the specified loadings cases are applied. For loading, this work applied six macroscopic strains,  $\epsilon_{xx}$ ,  $\epsilon_{yy}$ ,  $\epsilon_{zz}$ ,  $\epsilon_{xy}$ ,  $\epsilon_{xz}$ ,  $\epsilon_{yz}$  (pure x, y, z tension and xy, yz, zx shear.) on the RVE to obtain the six unknown components of the stiffness matrix.

Generally, the elasto-plastic responses of the composites include the uniaxial tension and shear behaviors. For predicting the shear elasto-plastic behaviors of the composites, the corresponding formulas first PBC are the same as those (Eq. (16) – (20)) used to calculate the elastic properties. However, the PBC used to predict the uniaxial elasto-plastic response of the composites should obey the zero macro-stress constraints:

$$\oint_{\omega} \sigma_{ii} dV_{RVE} = 0, \oint_{\omega} \sigma_{jj} dV_{RVE} = 0, \quad (21)$$

where  $\sigma_{ii}$  and  $\sigma_{jj}$  are the stress in the direction  $i$  and  $j$ . Therefore, the PBC formulas used to calculate uniaxial tensile elasto-plastic are not the same

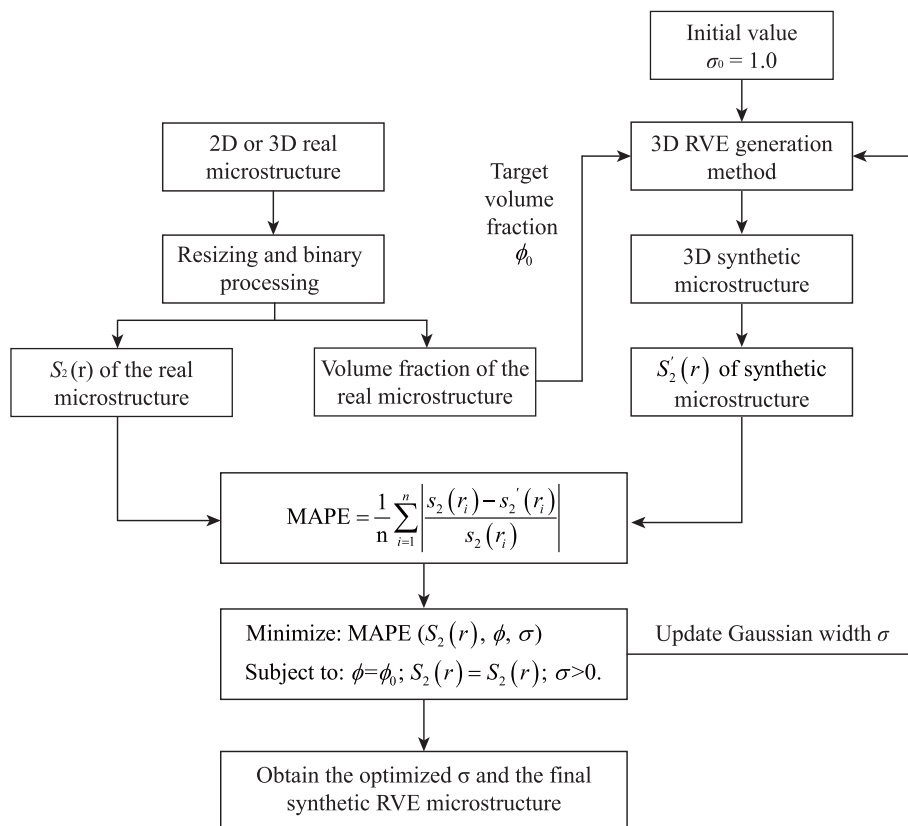


**Fig. 7.** Flowchart of the synthetic RVE generation from real microstructures.

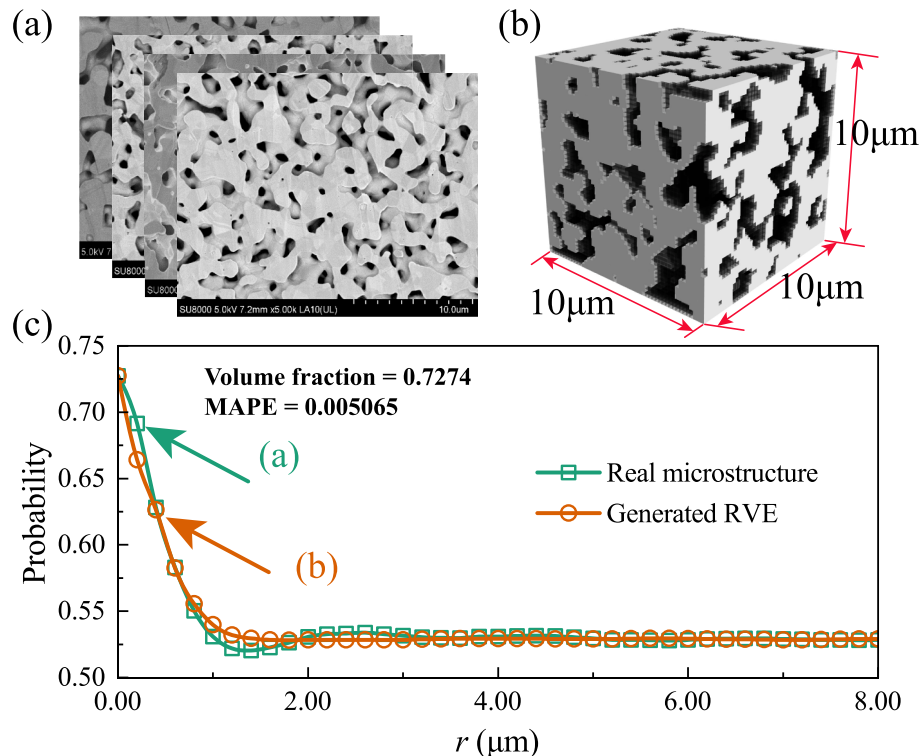


**Fig. 8.** Microstructures and two-point probability functions of sintered metal particles: (a) real microstructure, (b) generated RVE, and (c) two-point probability functions of real microstructure and generated RVE.

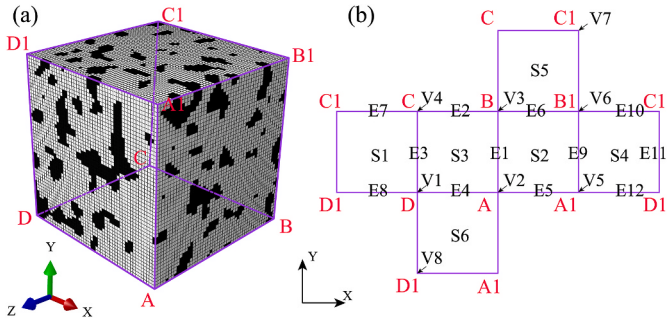


**Fig. 9.** (a) Category for node set on the surface of the meshed composites RVE and (b) planar notation.

as Eq. 16–20 and the detailed expression of the PBC for predicting the uniaxial tensile elasto-plastic responses are written as follows.

#### I. Surface nodes:

a. Surface left S1 to Surface right S2:

$$u_x^{ABB1A1} - u_x^{CDD1C1} = \bar{\epsilon}_{xx}, u_y^{ABB1A1} - u_y^{CDD1C1} = 0, u_z^{ABB1A1} - u_z^{CDD1C1} = 0. \quad (22)$$

b. Surface top S4 to Surface bottom S3:

$$u_x^{A1B1C1D1} - u_x^{ABCD} = 0, u_y^{A1B1C1D1} - u_y^{ABCD} = \bar{\epsilon}_{yy}, u_z^{A1B1C1D1} - u_z^{ABCD} = 0. \quad (23)$$

c. Surface front S6 to Surface back S5:

$$u_x^{ADD1A1} - u_x^{BCC1B1} = 0, u_y^{ADD1A1} - u_y^{BCC1B1} = 0, u_z^{ADD1A1} - u_z^{BCC1B1} = \bar{\epsilon}_{zz}. \quad (24)$$

#### II. Edge nodes:

$$\begin{aligned} u_x^{A1D1} - u_x^{AD} = 0, u_x^{AD} - u_x^{BC} = 0, u_x^{A1D1} - u_x^{AD} = 0, \\ u_y^{AA1} - u_y^{DD1} = 0, u_y^{DD1} - u_y^{CC1} = 0, u_y^{BB1} - u_y^{AA1} = 0, \\ u_z^{AB} - u_z^{CD} = 0, u_z^{A1B1} - u_z^{C1D1} = 0, u_z^{CD} - u_z^{C1D1} = 0, \end{aligned} \quad (25)$$

#### III. Vertex nodes:

$$\begin{aligned} u_x^{A1} - u_x^+ = 0, u_x^{A1} = u_x^{B1} = u_x^B = u_x^A = u_x^{A1B1} = u_x^{AB} = u_x^{AA1} = u_x^{BB1} = u_x^{AA1B1B}, \\ u_x^{D1} - u_x^- = 0, u_x^{D1} = u_x^{C1} = u_x^C = u_x^D = u_x^{C1D1} = u_x^{CD} = u_x^{DD1} = u_x^{CC1} = u_x^{D1C1CD}, \\ u_y^{D1} - u_y^+ = 0, u_y^{D1} = u_y^{A1} = u_y^{B1} = u_y^{C1} = u_y^{D1A1} = u_y^{A1B1} = u_y^{B1C1} = u_y^{C1D1} = u_y^{A1B1C1D1}, \\ u_y^D - u_y^- = 0, u_y^D = u_y^A = u_y^B = u_y^C = u_y^{DA} = u_y^{AB} = u_y^{BC} = u_y^{CD} = u_y^{ABCD}, \\ u_z^{D1} - u_z^+ = 0, u_z^{D1} = u_z^{A1} = u_z^A = u_z^D = u_z^{D1A1} = u_z^{AA1} = u_z^{AD} = u_z^{DD1} = u_z^{D1A1AD}, \\ u_z^{C1} - u_z^- = 0, u_z^{C1} = u_z^{B1} = u_z^B = u_z^C = u_z^{C1B1} = u_z^{BB1} = u_z^{BC} = u_z^{CC1} = u_z^{B1CC1}, \end{aligned} \quad (26)$$

where  $u_i^+$  and  $u_i^-$  are the reference strains and contribute to applying three uniaxial loading conditions of the RVE composites, which are given as follows:

$$\epsilon_{xx}^* = u_x^+ - u_x^-, \epsilon_{yy}^* = u_y^+ - u_y^-, \epsilon_{zz}^* = u_z^+ - u_z^-. \quad (27)$$

It should be noted that all PBCs for the elastic and elasto-plastic behaviors of the composites are implemented via a Python script in the ABAQUS. In addition, the maximum plastic strain should less than 1% of the length of the RVE to ensure no damage occurs.

#### 4. Results and discussion

Sintered AgNPs with a random quasi-continuous porous microstructure, as one of the typical MMNCs, are investigated in this work. The mechanical behavior of sintered AgNPs is highly sensitive to variations in the matrix volume fraction and pore size. The Ag volume fraction, which is equivalent to 1 minus the porosity, plays a critical role in determining the mechanical response of this dual-phase microstructure. Additionally, we investigate the effect of pore size by varying the Gaussian width, providing insights into the impact of pore size on the mechanical properties. The elasto-plastic property of the Ag in the matrix phase follows a power-law constitutive model as [47]:

$$\sigma = \begin{cases} E\epsilon, \epsilon \leq \epsilon_y \\ Re^n, \epsilon > \epsilon_y \end{cases}, \quad (28)$$

where the elastic modulus  $E$  is 80.0 GPa, the hardening coefficient  $R$  is 0.655 GPa, the hardening exponent  $n$  is 0.235, the yield strain  $\epsilon_y$  is 0.1875 corresponding to the yield stress  $\sigma_y$  of 150 MPa, and the ultimate tensile strength is 300 MPa for the pure Ag without any pores. Besides, the remaining phase of the RVE, pores, have a negligible elastic modulus. The length of the cubic RVE of the sintered AgNPs is 10.0 μm and the mesh size is 0.2 μm. On the surfaces of the RVEs, six types of monotonic loading conditions, including pure  $x$ ,  $y$ , and  $z$  tension and pure  $xy$ ,  $xz$ , and  $yz$  shear, were used to predict the elasto-plastic properties of the sintered AgNPs. Fig. 10 shows the von Mises stress of the RVE of sintered AgNPs under these six loading conditions under the small deformation limitation (1%). Under PBCs for pure tension and shear, stress-concentrated zones are networked differently in the RVE. Since the RVEs could be nearly considered as isotropic mechanical properties, under small deformation constraints, the stress distributions in their loading directions of the pure tension (Fig. 10(a)–(c)) and pure shear loadings (Fig. 10(d)–(f)) are similar.

##### 4.1. Effect of the ratio of Gaussian width

The reinforcement size, that is the pore size of the RVE of sintered AgNPs composites, is depended on the Gaussian width. A larger size would increase the uncertainty of the resulting elasto-plastic properties of the RVE due to the randomness of Gaussian algorithm. Therefore, the appropriate Gaussian width  $\sigma$  should be specified firstly. A set of RVEs with different width ratio  $\sigma/L$  are generated and implemented to obtained the effective elastic properties (Fig. 11). Meanwhile, the errors among the resulting RVEs with the same width ratio are calculated to evaluate the consistency of the models, which is written as:

$$\text{error}(\%) = \frac{E_{\max} - E_{\min}}{N_{RVEs}} \cdot 100\%, \quad (29)$$

$$\frac{1}{N_{RVEs}} \sum_{i=1}^{N_{RVEs}} E_i$$

where  $E_{\max}$  and  $E_{\min}$  are the maximum and minimum elastic properties of the RVEs with the same Gaussian width  $\sigma$  and matrix volume fraction.  $N_{RVEs}$  is the number of the RVEs generated for each Gaussian width  $\sigma$  and matrix volume fraction. When the  $\sigma/L$  increases from 0.1 to 0.5, the elastic properties, such as the elastic modulus, Poisson's ratio and shear modulus tend to decrease. Conversely, the elastic property errors increase. Moreover, the matrix volume fractions also influence the error of the elastic properties, and a large matrix volume fraction contributes to the stabilization of the elastic properties and reduces the error of the elastic properties. Accordingly, an appropriate Gaussian width  $\sigma$  should be determined by taking both the matrix volume fraction and reinforcement size of MMNCs into account. Therefore, for the sintered AgNPs with a matrix volume fraction of 0.70–1.00, the Gaussian width  $\sigma$  is set to 1.5, corresponding to  $\sigma/L$  of 0.30 and the tolerable error threshold of 3.0%

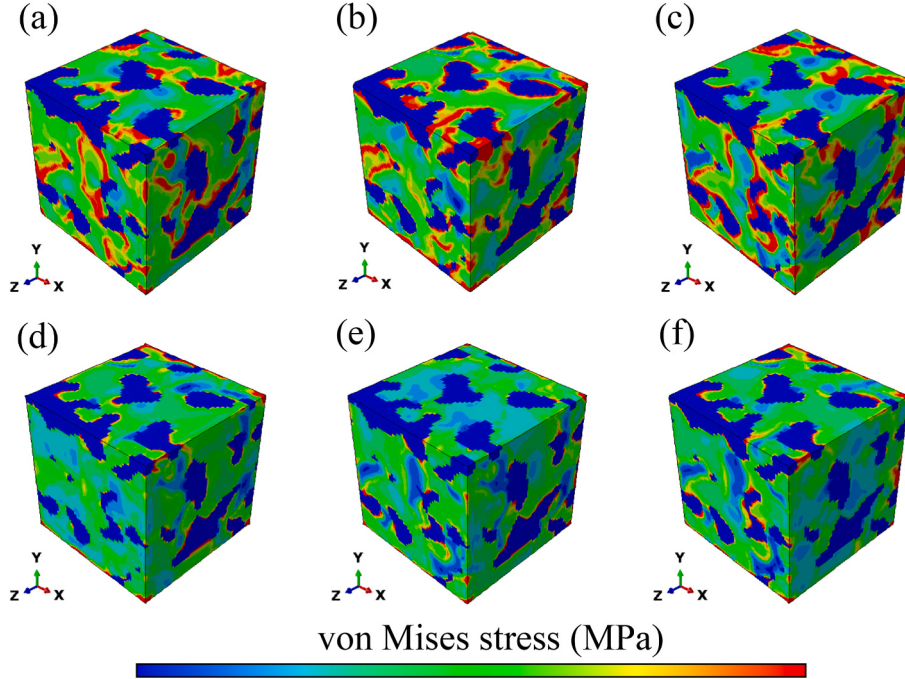


**Fig. 10.** Stress distributions of the RVE for six types of monotonic loading conditions, (a) pure  $x$  tension, (b) pure  $y$  tension, (c) pure  $z$  tension, (d) pure  $xy$  shear, (e) pure  $xz$  shear and (f) pure  $yz$  shear.

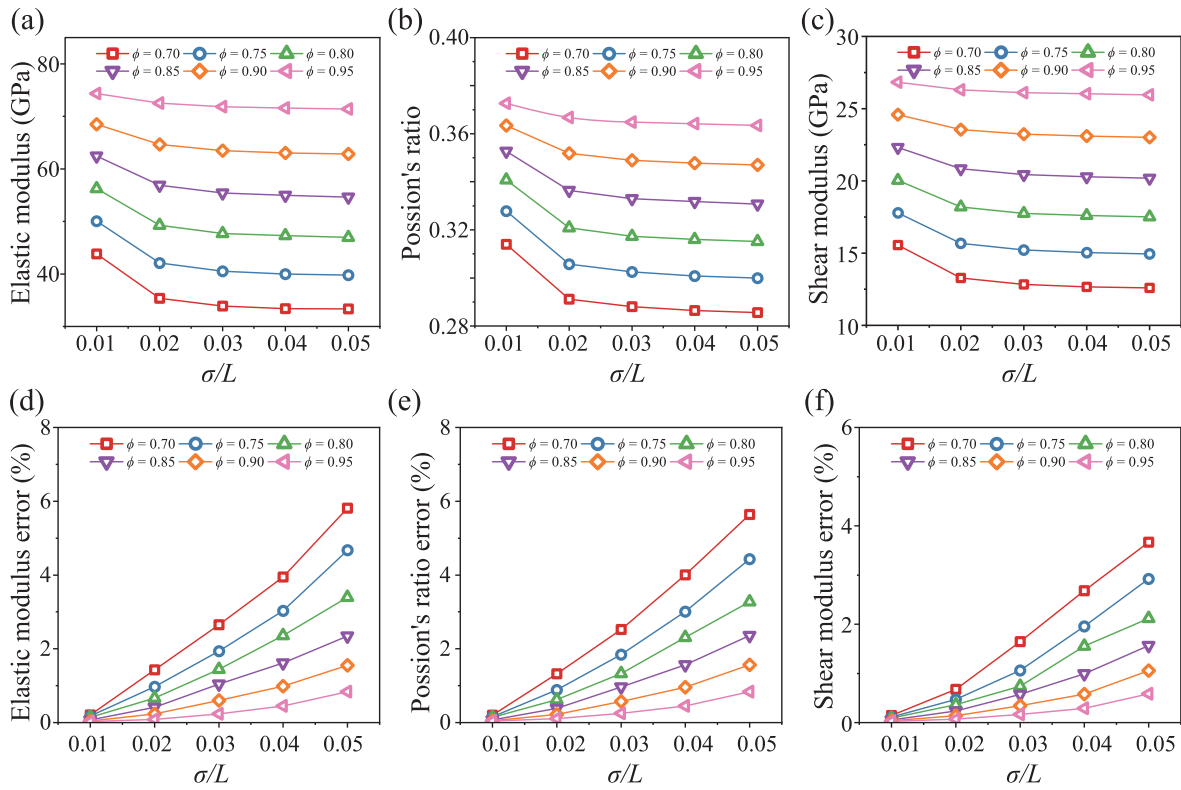


**Fig. 11.** Elastic properties and their errors of the sintered AgNPs composites regarding the ratio of Gaussian width to edge length  $\sigma/L$ , (a)–(c) elastic modulus, Poisson's ratio and shear modulus, (d)–(f) elastic modulus error, Poisson's ratio error, and shear modulus error.

#### 4.2. Elastic properties of MMNCs

The elastic properties of the RVE of MMNCs are calculated with a wide range of matrix volume fractions from 0.7 to 1.0. Fig. 12 shows the effective elastic modulus, Poisson's ratio, shear modulus, and the

relative errors among the RVEs with the same matrix volume fraction.

As the matrix volume fraction increases, the elastic modulus of the AgNPs composites increases approximately linearly from 33.86 MPa to 80.61 MPa, while the errors of the elastic modulus reduce from 2.65% to 0.09% (Fig. 12 (a)). Here, Kähler et al. [48] investigated the correlation

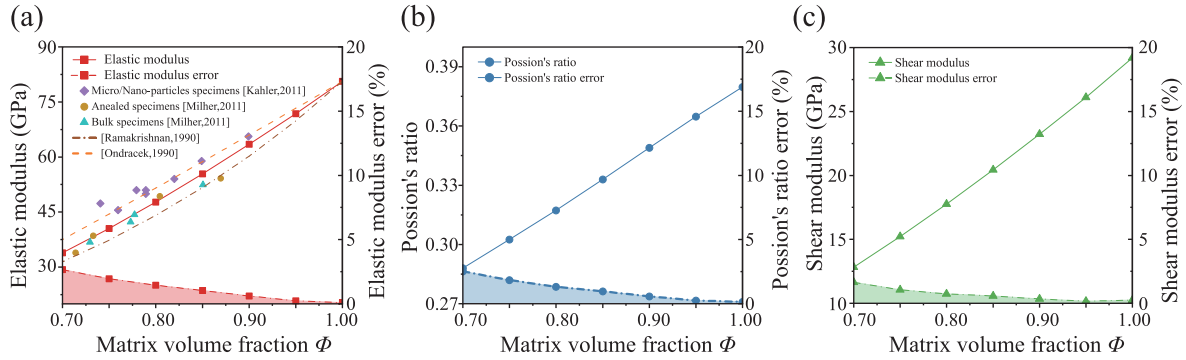


**Fig. 12.** Elastic properties of the sintered AgNPs with matrix volume fraction from 0.70 to 1.00, (a) elastic modulus and its error [48–51], (b) Poisson's ratio and its error, (c) shear modulus and its error.

between porosity and elastic modulus of sintered silver particles with varying particle sizes. Milhet et al. [49] also examined the impact of porosity on the elastic properties of sintered Ag paste in both bulk and joint specimens. Our work utilized the RVE based FE homogenization approach, as demonstrated in Fig. 12(a), the resulting elastic moduli agreed closely with experimental measurements of the reported works.

Moreover, the resulting elastic properties are also compared with the analytical models of sintered porous Ag proposed by Ondracek [50] and Ramakrishnan [51], respectively:

$$E = E_{Ag} \frac{3(3 - 5p)(1 - p)}{9 - p(9.5 - 5.5V_{Ag})}, \quad (30)$$

$$E = E_{Ag} \frac{(1 - p)^2}{1 + p(2 - 3V_{Ag})}, \quad (31)$$

where  $E_{Ag}$  and  $V_{Ag}$  are the elastic modulus and Poisson's ratio of bulk silver,  $p$  is the density of sintered porous Ag. It is found that the elastic moduli of the RVE of the AgNPs composites are basically consistent with those of the analytical models.

In Fig. 12 (b) and (c), it is found that both the Poisson's ratio and shear modulus increase with the matrix volume fraction, where Poisson's ratio rises from 0.29 to 0.38 and the shear modulus grows from 12.83 GPa to 29.19 GPa. In addition, the error of the Poisson's ratio reduces from 1.64% to 0.24%, and the error of the shear modulus declines from 2.52% to 0.14%.

#### 4.3. Elasto-plastic responses of dual-phase MMNCs

To validate the capacity of the RVE-based numerical homogenization method proposed in this work, a set of RVEs of the AgNPs composites with the matrix volume fractions of 0.70, 0.80, and 0.90 are generated and implemented to capture the effective elasto-plastic response in the

$x$ -,  $y$ -, and  $z$ -directions. It is noted that the ratio of the Gaussian widths to the RVE length  $\sigma/L$  is the same as the previous section.

It is found that in Fig. 13, due to the enhancement effect of the matrix, in the elastic deformation stage, the elastic modulus (slope of the curves) increases with the matrix volume fraction. The middle parts of the  $\epsilon - \sigma$  curves demonstrate that the effective stresses of the plastic zones in different directions become greater with the volume fraction increases. It is because the RVE with a larger matrix volume fraction involves more solid material points to achieve the greater ultimate tensile strength under the same total strain. The more complex microstructures would lead to different mechanical responses in various directions. In contrast, the stresses of RVEs with small matrix volume fractions are relatively stable because the pores absorb a large amount of deformation. Therefore, according to the almost identical elasto-plastic responses in different directions ( $x$ ,  $y$ ,  $z$ ) at the small deformation/strain range (<1%), it is reasonable to consider the RVE almost as isotropic domain. In addition, it should be noted that the UTS of pure silver with zero porosity is 0.3 GPa. The UTS of the RVEs with high volume fraction exhibits reinforcement in some directions, albeit the mean value is less than 0.3 GPa. On the other hand, the UTS of RVEs with smaller matrix volume fractions are less than 0.3 GPa, showing a notable decrease as the volume fraction decreases.

#### 5. Conclusion

In this work, we proposed a new algorithm for generating the RVE and evaluating the effective mechanical properties of MMNCs with quasi-continuous volume distribution microstructures, which combining the Gaussian filtering methods and fraction cutting levels algorithms. Meanwhile, the PBCs are imposed on the RVE via the Python script to investigate the effective elastic/elasto-plastic properties of sintered AgNPs MMNCs. Several conclusions of this work are drawn as follows:

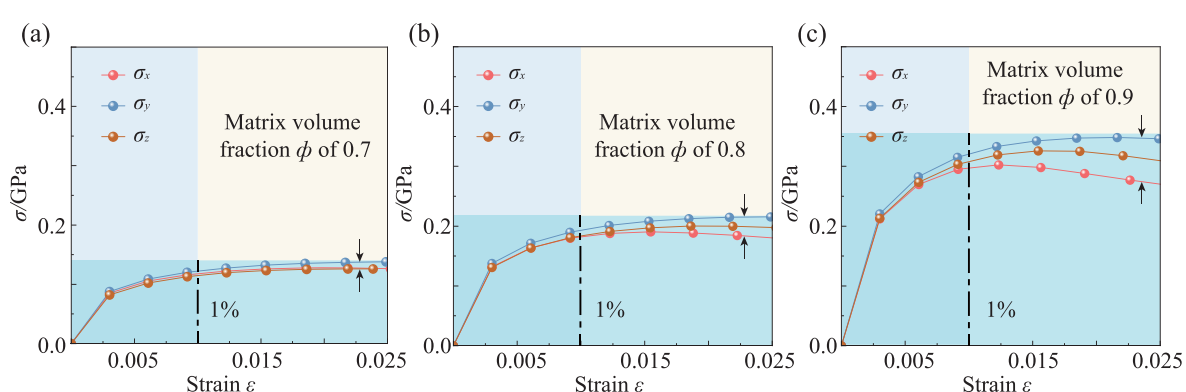


**Fig. 13.** Elasto-plastic responses of the RVE of AgNPs composites under pure tensile loads in  $x$ ,  $y$ , and  $z$  directions with different matrix volume fractions.

- (1) The proposed algorithm can control the size distribution of the reinforcement and the matrix volume fractions by adjusting the Gaussian width and cutting level. In addition, the individual point-controlled quantile functions can achieve a quasi-continuous volume fraction.
- (2) The ratio of  $\sigma/L$  influences the stability and robustness of the evaluated elasto-plastic properties of the dual-phase MMNCs. Specifically for the sintered AgNPs composites, a ratio  $\sigma/L$  smaller than 2.5 could ensure the reliable results.
- (3) The resulting elastic and elasto-plastic responses of the RVEs of sintered AgNPs composites with matrix volume fractions ranging from 0.7 to 1.0, are agreed well with the experimental results and the analytical models.

#### CRediT authorship contribution statement

**Yutai Su:** Software, Validation, Investigation, Data curation, Writing – original draft. **Ziyi Shen:** Conceptualization, Writing – review & editing, Writing – original draft. **Xu Long:** Software, Funding acquisition, Supervision. **Chuantong Chen:** Conceptualization, Methodology. **Lehua Qi:** Writing – review & editing, Supervision, Funding acquisition. **Xujiang Chao:** Conceptualization, Methodology, Validation, Investigation, Writing – review & editing, Supervision.

#### Declaration of competing interest

The authors declare that they have no known competing financial interests or personal relationships that could have appeared to influence the work reported in this paper.

#### Data availability

Data will be made available on request.

#### Acknowledgements

The authors are very grateful for the financial support from the National Natural Science Foundation of China (No. 51972271, 52231004, 52175148), the Natural Science Foundation of Chongqing (No. CSTB2022NSCQ-MSX0574), the Fundamental Research Funds for the Central Universities (No. D5000220523), the National Key Laboratory Foundation 2022-JCJQ-LB-006 (No. 6142411232212), and the Shock and Vibration of Engineering Materials and Structures Key Laboratory of Sichuan Province (No. 22kfgk04).

#### Appendix A. Supplementary data

Supplementary data to this article can be found online at <https://doi.org/10.1016/j.msea.2023.145001>.

#### References

- [1] S.C. Tjong, Recent progress in the development and properties of novel metal matrix nanocomposites reinforced with carbon nanotubes and graphene nanosheets, *Mater Sci Eng: Inside R* 74 (10) (2013) 281–350.
- [2] X.M. Mei, Q.S. Mei, Y.Q. Peng, Z.H. Chen, T. Xu, Y.C. Wang, Achieving enhanced mechanical properties of SiC/Al–Cu nanocomposites via simultaneous solid-state alloying of Cu and dispersing of SiC nanoparticles, *Mater. Sci. Eng., A* 860 (2022), 144338.
- [3] Y. Zhu, K. Ameyama, P.M. Anderson, I.J. Beyerlein, H. Gao, H.S. Kim, E. Lavernia, S. Mathaudhu, H. Mughrabi, R.O. Ritchie, N. Tsuji, X. Zhang, X. Wu, Heterostructured materials: superior properties from hetero-zone interaction, *Mater Res Lett* 9 (1) (2021) 1–31.
- [4] W.H. Yu, S.L. Sing, C.K. Chua, C.N. Kuo, X.L. Tian, Particle-reinforced metal matrix nanocomposites fabricated by selective laser melting: a state of the art review, *Prog. Mater. Sci.* 104 (2019) 330–379.
- [5] M. Sabzevari, R.J. Teymoori, S.A. Sajjadi, FE modeling of the compressive behavior of porous copper-matrix nanocomposites, *Mater. Des.* 86 (2015) 178–183.
- [6] F. Lin, F. Jia, M. Ren, J. Wang, M. Yang, Z. Chen, Z. Jiang, Microstructure, mechanical and thermal properties of ultrafine-grained Al2024–TiC-GNPs nanocomposite, *Mater. Sci. Eng., A* 841 (2022), 142855.
- [7] L. Huang, M. Qian, Z. Liu, V.T. Nguyen, L. Yang, L. Wang, J. Zou, In situ preparation of TiB nanowires for high-performance Ti metal matrix nanocomposites, *J. Alloys Compd.* 735 (2018) 2640–2645.
- [8] S. Pan, K. Jin, T. Wang, Z. Zhang, L. Zheng, N. Umehara, Metal matrix nanocomposites in tribology: manufacturing, performance, and mechanisms, *Friction* 10 (2022) 1596–1634.
- [9] H.J. Bong, H. Lim, M.-G. Lee, D.T. Fullwood, E.R. Homer, R.H. Wagoner, An RVE procedure for micromechanical prediction of mechanical behavior of dual-phase steel, *Mater. Sci. Eng., A* 695 (2017) 101–111.
- [10] L.T. Harper, C. Qian, T.A. Turner, S. Li, N.A. Warrior, Representative volume elements for discontinuous carbon fibre composites – Part 1: boundary conditions, *Compos. Sci. Technol.* 72 (2) (2012) 225–234.
- [11] O. Pierard, C. Friebel, I. Doghri, Mean-field homogenization of multi-phase thermo-elastic composites: a general framework and its validation, *Compos. Sci. Technol.* 64 (10) (2004) 1587–1603.
- [12] H. Tsukamoto, A mean-field micromechanical approach to design of multiphase composite laminates, *Mater. Sci. Eng., A* 528 (7) (2011) 3232–3242.
- [13] I.B. Üçel, P. Gudmundson, A statistical RVE model for effective mechanical properties and contact forces in lithium-ion porous electrodes, *Int. J. Solid Struct.* 244–245 (2022), 111602.
- [14] A.G. Kashkooli, A. Amirfazli, S. Farhad, D.U. Lee, S. Felicelli, H.W. Park, K. Feng, V. De Andrade, Z. Chen, Representative volume element model of lithium-ion battery electrodes based on X-ray nano-tomography, *J. Appl. Electrochem.* 47 (3) (2017) 281–293.
- [15] R. Xu, Y. Yang, F. Yin, P. Liu, P. Cloetens, Y. Liu, F. Lin, K. Zhao, Heterogeneous damage in Li-ion batteries: experimental analysis and theoretical modeling, *J. Mech. Phys. Solid.* 129 (2019) 160–183.
- [16] R. Hill, Elastic properties of reinforced solids: some theoretical principles, *J. Mech. Phys. Solid.* 11 (5) (1963) 357–372.
- [17] I.M. Gitman, H. Askes, L.J. Sluys, Representative volume: existence and size determination, *Eng. Fract. Mech.* 74 (16) (2007) 2518–2534.
- [18] W.J. Drugan, J.R. Willis, A micromechanics-based nonlocal constitutive equation and estimates of representative volume element size for elastic composites, *J. Mech. Phys. Solid.* 44 (4) (1996) 497–524.
- [19] X. Gao, X. Zhang, L. Geng, Strengthening and fracture behaviors in SiCp/Al composites with network particle distribution architecture, *Mater. Sci. Eng., A* 740–741 (2019) 353–362.
- [20] Y. Gao, Y. Jiao, Y. Liu, Ultra-efficient reconstruction of 3D microstructure and distribution of properties of random heterogeneous materials containing multiple phases, *Acta Mater.* 204 (2021), 116526.
- [21] F.N. Dehnavi, M. Safdari, K. Abrinia, M. Baniassadi, Microstructural design of tunable elastoplastic two-phase random heterogeneous materials, *Mater. Today Commun.* 27 (2021), 102300.
- [22] L.T. Fan, S.J. Chen, C.A. Watson, ANNUAL REVIEW solids mixing, *Ind. Eng. Chem.* 62 (7) (1970) 53–69.
- [23] A.W. Nienow, M.F. Edwards, N. Harnby, *Mixing in the Process Industries*, Butterworth-Heinemann, 1997.
- [24] S. Torquato, Author, H.W. Haslach, Random heterogeneous materials: microstructure and macroscopic properties, *Appl. Mech. Rev.* 55 (4) (2002) B62–B63.
- [25] A. Rogers, *Statistical Analysis of Spatial Dispersion, The quadrat method*, 1974.
- [26] M. Jahedi, E. Ardjmand, M. Knezevic, Microstructure metrics for quantitative assessment of particle size and dispersion: application to metal-matrix composites, *Powder Technol.* 311 (2017) 226–238.
- [27] W. Tian, X. Chao, M.W. Fu, L. Qi, An advanced method for efficiently generating composite RVEs with specified particle orientation, *Compos. Sci. Technol.* 205 (2021), 108647.
- [28] C.J. Permann, D.R. Gaston, D. Andrš, R.W. Carlsen, F. Kong, A.D. Lindsay, J. M. Miller, J.W. Peterson, A.E. Slaughter, R.H. Stogner, R.C. Martineau, MOOSE: enabling massively parallel multiphysics simulation, *SoftwareX* 11 (2020), 100430.
- [29] S. Falco, N. Fogell, S. Kasinos, L. Iannucci, Homogenisation of micromechanical modelling results for the evaluation of macroscopic material properties of brittle ceramics, *Int. J. Mech. Sci.* 220 (2022), 107071.
- [30] R. Quey, Neper: a 3-D Random Polycrystal Generator for the Finite Element Method, 2009.
- [31] Y. Liu, S.-T. Quek, F.-H. Lee, Translation random field with marginal beta distribution in modeling material properties, *Struct. Saf.* 61 (2016) 57–66.
- [32] J.W. Boley, E.L. White, R.K. Kramer, Mechanically Sintered Gallium–Indium Nanoparticles 27 (14) (2015) 2355–2360.
- [33] S. Zabihzadeh, S. Van Petegem, M. Holler, A. Diaz, L.I. Duarte, H. Van Swygenhoven, Deformation behavior of nanoporous polycrystalline silver. Part I: microstructure and mechanical properties, *Acta Mater.* 131 (2017) 467–474.
- [34] Y. Su, J. Zhu, X. Long, L. Zhao, C. Chen, C. Liu, Statistical effects of pore features on mechanical properties and fracture behaviors of heterogeneous random porous materials by phase-field modeling, *Int. J. Solid Struct.* 264 (2023), 112098.
- [35] C. Ding, H. Liu, K.D.T. Ngo, R. Burgos, G.Q. Lu, A double-side cooled SiC MOSFET power module with sintered-silver interposers: I-design, simulation, fabrication, and performance characterization, *IEEE Trans. Power Electron.* 36 (10) (2021) 11672–11680.
- [36] A. Chiappone, M. Gillone, M. Castellino, K. Bejtka, K. Rajan, I. Roppolo, D. Perrone, S. Bocchini, C. Ricciardi, C.F. Pirri, A. Chiolerio, In situ generation of

- silver nanoparticles in PVDF for the development of resistive switching devices, *Appl. Surf. Sci.* 455 (2018) 418–424.
- [37] V. Sanchez-Romaguera, S. Wünscher, B.M. Turki, R. Abbel, S. Barbosa, D.J. Tate, D. Oyeka, J.C. Batchelor, E.A. Parker, U.S. Schubert, S.G. Yeates, Inkjet printed paper based frequency selective surfaces and skin mounted RFID tags: the interrelation between silver nanoparticle ink, paper substrate and low temperature sintering technique, *J. Mater. Chem. C* 3 (9) (2015) 2132–2140.
- [38] K. Sugiura, T. Iwashige, K. Tsuruta, C. Chen, S. Nagao, T. Funaki, K. Suganuma, Reliability evaluation of SiC power module with sintered Ag die attach and stress-relaxation structure, *IEEE transactions on components, Packag Manuf Tech* 9 (4) (2019) 609–615.
- [39] C. Chen, S. Nagao, K. Suganuma, J. Jiu, T. Sugahara, H. Zhang, T. Iwashige, K. Sugiura, K. Tsuruta, Macroscale and microscale fracture toughness of microporous sintered Ag for applications in power electronic devices, *Acta Mater.* 129 (2017) 41–51.
- [40] X. Guo, Q. Guo, J. Nie, Z. Liu, Z. Li, G. Fan, D.-B. Xiong, Y. Su, J. Fan, D. Zhang, Particle size effect on the interfacial properties of SiC particle-reinforced Al-Cu-Mg composites, *Mater. Sci. Eng., A* 711 (2018) 643–649.
- [41] K. Munir, C. Wen, Y. Li, Graphene nanoplatelets-reinforced magnesium metal matrix nanocomposites with superior mechanical and corrosion performance for biomedical applications, *J. Magnesium Alloys* 8 (1) (2020) 269–290.
- [42] N.S. Mohd Zubir, H. Zhang, G. Zou, H. Bai, Z. Deng, B. Feng, A. Wu, L. Liu, Y. N. Zhou, Large-area die-attachment sintered by organic-free Ag sintering material at low temperature, *J. Electron. Mater.* 48 (11) (2019) 7562–7572.
- [43] X.P. Li, G. Ji, Z. Chen, A. Addad, Y. Wu, H.W. Wang, J. Vleugels, J. Van Humbeeck, J.P. Kruth, Selective laser melting of nano-TiB<sub>2</sub> decorated AlSi10Mg alloy with high fracture strength and ductility, *Acta Mater.* 129 (2017) 183–193.
- [44] Y. Su, G. Fu, C. Liu, K. Zhang, L. Zhao, C. Liu, A. Liu, J. Song, Thermo-elasto-plastic phase-field modelling of mechanical behaviours of sintered nano-silver with randomly distributed micro-pores, *Comput. Methods Appl. Mech. Eng.* 378 (2021), 113729.
- [45] M. Hori, S. Nemat-Nasser, On two micromechanics theories for determining micro-macro relations in heterogeneous solids, *Mech. Mater.* 31 (10) (1999) 667–682.
- [46] W. Tian, L. Qi, X. Chao, J. Liang, M. Fu, Periodic boundary condition and its numerical implementation algorithm for the evaluation of effective mechanical properties of the composites with complicated micro-structures, *Compos. B Eng.* 162 (2019) 1–10.
- [47] X. Long, Q.P. Jia, Z. Li, S.X. Wen, Reverse analysis of constitutive properties of sintered silver particles from nanoindentations, *Int. J. Solid Struct.* 191–192 (2020) 351–362.
- [48] J. Kähler, N. Heuck, G. Palm, A. Stranz, A. Waag, E. Peiner, Low-pressure sintering of silver micro- and nanoparticles for a high temperature stable pick & place die attach, in: 18th European Microelectronics & Packaging Conference, 2011, pp. 1–7.
- [49] X. Milhet, P. Gadaud, V. Caccuri, D. Bertheau, D. Mellier, M. Gerland, Influence of the porous microstructure on the elastic properties of sintered Ag paste as replacement material for die attachment, *J. Electron. Mater.* 44 (10) (2015) 3948–3956.
- [50] G. Ondracek, On the relationship between the properties and the microstructure of multiphase materials Pt 3, *Zeitschrift fuer Werkstofftechnik* 9 (3) (1978) 96–100.
- [51] N. Ramakrishnan, V.S. Arunachalam, Effective elastic moduli of porous solids, *J. Mater. Sci.* 25 (9) (1990) 3930–3937.